

A numerical assessment of simple airblast models of impact airbursts

Gareth S. COLLINS* , Elliot LYNCH, Ronan McADAM, and Thomas M. DAVISON 

Department of Earth Science and Engineering, Impact and Astromaterials Research Centre, Imperial College,
London SW7 2AZ, UK

*Corresponding author. E-mail: g.collins@imperial.ac.uk

(Received 17 August 2016; revision accepted 02 March 2017)

Abstract—Asteroids and comets 10–100 m in size that collide with Earth disrupt dramatically in the atmosphere with an explosive transfer of energy, caused by extreme air drag. Such airbursts produce a strong blastwave that radiates from the meteoroid's trajectory and can cause damage on the surface. An established technique for predicting airburst blastwave damage is to treat the airburst as a static source of energy and to extrapolate empirical results of nuclear explosion tests using an energy-based scaling approach. Here we compare this approach to two more complex models using the iSALE shock physics code. We consider a moving-source airburst model where the meteoroid's energy is partitioned as two-thirds internal energy and one-third kinetic energy at the burst altitude, and a model in which energy is deposited into the atmosphere along the meteoroid's trajectory based on the pancake model of meteoroid disruption. To justify use of the pancake model, we show that it provides a good fit to the inferred energy release of the 2013 Chelyabinsk fireball. Predicted overpressures from all three models are broadly consistent at radial distances from ground zero that exceed three times the burst height. At smaller radial distances, the moving-source model predicts overpressures two times greater than the static-source model, whereas the cylindrical line-source model based on the pancake model predicts overpressures two times lower than the static-source model. Given other uncertainties associated with airblast damage predictions, the static-source approach provides an adequate approximation of the azimuthally averaged airblast for probabilistic hazard assessment.

INTRODUCTION

The breakup of a large asteroid or comet (meteoroid) due to aerodynamic stresses releases the majority of the meteoroid's kinetic energy into the atmosphere (Artemieva and Shuvalov 2016). As the meteoroid breaks up, the surface area exposed to the air increases and the body's retardation and fragmentation increases exponentially—resulting in an explosive release of energy (Passey and Melosh 1980; Chyba et al. 1993; Collins et al. 2005). The largest airbursts release energies in the megaton (Mt) to tens-of-megatons range (one ton of TNT is equivalent to 4.184 gigajoules, 4.184×10^9) and, if the majority of the energy release occurs sufficiently low in the atmosphere, the strength of the resultant atmospheric blast wave can cause damage on the ground. Examples of such airbursts include the 3–15 Mt, 1908

Tunguska event, which caused extensive tree damage over a 2200 km² area (e.g., Ben-Menahem 1975; Chyba et al. 1993; Boslough and Crawford 2008; Artemieva and Shuvalov 2016) and more recently the ~0.5 Mt, 2013 Chelyabinsk fireball, which occurred over a densely populated region of Russia, injuring more than 1600 people and breaking windows in the surrounding towns (Popova et al. 2013). Although often less damaging than crater-forming impacts, airbursts are far more common—with a Tunguska-scale event expected to have an average recurrence interval in the range 100–2000 yr (Brown et al. 2013).

As atmospheric nuclear explosions have been observed to produce blast waves similar to those observed or inferred for impact airbursts (Glasstone and Dolan 1977), an established technique for fast calculation of airburst blastwave damage is to treat the airburst as a

static source of energy, equivalent to a nuclear explosion (e.g., Toon et al. 1997; Collins et al. 2005). For instance, the protocol adopted by Collins et al. (2005) comprises three parts (1) a model of atmospheric disruption to determine the approximate burst altitude and energy (the pancake model), (2) a scaling procedure for relating the airburst scenario (burst altitude and energy) to a representative static 1 kt nuclear explosion scenario (yield scaling), and (3) a database of nuclear test data documenting blast pressure as a function of range for static 1 kt atmospheric explosions at a range of altitudes (Glasstone and Dolan 1977). A simple approach such as this is required for probabilistic impact hazard assessment, in which hundreds of thousands of scenarios must be considered (e.g., Reinhardt et al. 2016).

Although the static-source approximation is a good representation of nuclear blast waves, it has limitations when applied to meteor phenomenon (Collins et al. 2005; Boslough and Crawford 2008; Shuvalov et al. 2013). The most obvious limitation of the approximation in this context is that the source is static, whereas at peak energy release, a meteor is still moving at hypersonic velocities—considerably faster than the speed at which the blast wave propagates—suggesting that the static explosion analogy may underestimate blast damage on the ground (Boslough and Crawford 2008). In addition, recent data from Chelyabinsk (Popova et al. 2013) suggest elliptical-shaped blast damage contours with semimajor axes perpendicular to the trajectory, which contrasts with the circular peak pressure contours predicted by the static-source model.

In this paper, we re-examine the static-source approximation as a procedure for estimating airburst blast damage using numerical modeling. First, we use a fast, semianalytical approximation of the pancake model of a meteoroid's atmospheric disruption—modified to account for meteoroid ablation—to constrain the range and likelihood of airburst altitude/energy combinations and the residual kinetic energy of the meteoroid at burst. We show that the 2013, ~500 kt Chelyabinsk airburst can be well described using the pancake model and occurred at an altitude several kilometers higher than the worst-case scenario expected for this energy range. Second, we use the iSALE2D shock physics code to simulate blastwave formation, attenuation, and interaction with the surface under three simple energy deposition approximations: a spherical static source of internal energy equivalent to the impact energy, a spherical moving source with a one-third kinetic-to-internal energy partitioning, and a cylindrical line source with the energy per unit path length determined by the pancake model. We compare the results of our simulations to observations and detailed hydrodynamic simulation of meteoroid

disruption in the atmosphere (Shuvalov et al. 2013) to establish the strengths and weaknesses of each modeling approach. Our focus is to refine protocols for fast estimation of airburst blastwave damage on the ground that can be used in probabilistic hazard assessment.

PANCAKE MODEL OF METEOROID DISRUPTION IN THE ATMOSPHERE

The motion of a meteoroid through the atmosphere and mass loss owing to ablation can be described by a set of four ordinary differential equations (e.g., Passey and Melosh 1980) up to the point that the meteoroid fragments. Fragmentation is commonly assumed to occur when the ram pressure in front of the meteoroid (the local air density times the meteoroid velocity squared), exceeds the meteoroid's strength. Beyond the fragmentation point, an additional equation is required to describe the increase in cross-sectional area of the disrupted rock mass as it deforms in response to aerodynamic stresses, decelerates, and penetrates denser air (e.g., Chyba et al. 1993; Hills and Goda 1993; Avramenko et al. 2014).

In the “pancake model” (Chyba et al. 1993; Collins et al. 2005), the spreading rate is defined by a force balance on the walls of the disrupted meteoroid, which is approximated as an incompressible, strengthless cylinder, deformed by an average differential stress proportional to the ram pressure. The name of the model refers to the tendency of the meteoroid to deform into a thin pancake-like cylinder with a large cross-sectional area. In an unconstrained pancake model, the meteoroid is allowed to expand without bound, while in a constrained model, the cylinder radius is limited to a multiple of the initial diameter of the meteor—the so-called pancake factor. In the similar “fragment cloud” model of Hills and Goda (1993) spreading rate is defined by equating the kinetic energy of the expanding fragments to the work done by the air to increase the area of the cloud of fragments. In this case, meteoroid spreading ceases when the ram pressure in front of the meteoroid drops below the strength of the meteoroid. Another, more recent meteoroid disruption model (Avramenko et al. 2014) derives an alternative spreading rate using dimensional analysis and a chain-reaction analogy for the cascading disruption of meteoroid fragments. Like the fragment cloud model, spreading is arrested when the ram pressure drops below the fragments' strength; however, in this case, the strength of the fragments is assumed to increase with time as fragment size decreases.

While these alternative models of meteoroid disruption and deceleration in the atmosphere differ somewhat in their prescriptions of spreading rate and

when spreading stops, in general they give similar results for a specific airburst scenario (e.g., Chelyabinsk; Avramenko et al. 2014; this work), depending on the choice of internal model parameters. The pancake model is considered here because it requires the fewest internal model parameters and because it forms the basis of an existing analytical approximation on which we build. However, in future work it would be instructive to compare all three models for a range of airburst scenarios to quantify the variability in their predictions.

Collins et al. (2005) derived an analytical approximation of the pancake model that neglects both gravitational acceleration and ablation. While the former is insignificant for meteoroids in the 10–100 m range, ablative loss of mass can be important. In Appendix A, we describe a modification to the analytical pancake model that approximates the effects of ablation. Using this procedure, the velocity and mass of the ablating and deforming meteoroid can be calculated as a function of altitude; and from these solutions, the kinetic energy lost by the meteoroid per kilometer can be determined for comparison with observed light-curve data. Figure 1 compares numerical solutions of the full pancake equations (dashed lines), both without (gray) and with (black) ablation, to the (semi-)analytical approximations (solid lines) of Collins et al. (2005), without ablation (gray), and presented here, with ablation (black). Figures 1a and 1b are for a Chelyabinsk-scale airburst scenario and a Tunguska-scale scenario, respectively. The pancake model parameters for both scenarios are given in Table 1. In both cases, accounting for ablation increases both the altitude and the magnitude of peak energy loss. Although the increases are less significant in the high-energy scenario, it is clear that accounting for the effects of ablation is important. The (semi-)analytical approximations of the pancake model underestimate the numerical solutions by ~20% in energy deposition per km for the Chelyabinsk-scale scenario, falling to ~10% for the higher energy, Tunguska-scale scenario. Given other uncertainties and the computational expediency of the approximation, this level of accuracy is acceptable for the purposes of quick hazard assessment.

Brown et al. (2013) concluded that the energy deposition predicted by the pancake model for Chelyabinsk is inconsistent with that derived from light-curve data. However, within the observational constraints for the Chelyabinsk impactor, we obtain a reasonable fit to the observed deposition curves with an unconstrained pancake model, and a good fit using a maximum pancake factor of 5–6 (Fig. 2a). For a constrained pancake model with maximum pancake factors <4 the fit is poor; in these cases, the meteoroid's deceleration is too gentle and its kinetic energy is

transferred to the atmosphere over too great a distance, resulting in a peak energy deposition that is much weaker and closer to the surface than inferred from observations. In a higher energy, Tunguska-scale scenario, pancake model predictions of energy deposition are less sensitive to the maximum pancake factor (Fig. 2b) so long as it exceeds ~4.

An important criticism of the pancake model is that, in its unconstrained form, it results in nonphysical geometries for the deformed meteor (Artemieva and Pierazzo 2009). For example, at the point of peak energy deposition, the 19 m Chelyabinsk bolide in Fig. 2a deforms to a 140 m wide dish with a thickness of less than half a meter. However, as we show, the unconstrained pancake model produces a reasonable fit to the energy deposition curves for Chelyabinsk. The implication is that the drag (effective cross-sectional area) predictions of the pancake model are correct even if the geometrical interpretation of the flattening cylinder is unphysical. The pancake model should thus be used in a similar manner to an empirical equation of state: to predict phenomena in regimes where it has been calibrated. In the case of high-energy airbursts, Chelyabinsk (~0.5 Mt) and Tunguska (3–15 Mt) provide the only calibration data and both of these (likely) involved stony asteroids. The pancake model should therefore be applied with caution outside of this range. Alternative models, such as the separate fragmentation model, provide a better description of a meteor's descent through the atmosphere for stronger or more dense impactors (Artemieva and Shuvalov 2001).

MONTE CARLO MODELING OF ASTEROID AIRBURSTS USING THE PANCAKE MODEL

Toon et al. (1997) used the pancake model to calculate airburst altitude as a function of energy for several impactor types (stone, carbonaceous, iron, and short- and long-period comets) and nominal impact parameters (angle and speed). In this section, we extend this analysis for noniron asteroids by applying the semianalytical approximation of the ablative pancake model equations to determine the most likely airburst altitude as a function of impact energy, and examine the uncertainty in this relationship, given the natural variability in impact angle and speed, as well as impactor density and strength.

Methodology

A data set of artificial airburst scenarios was created by means of a Monte Carlo simulation. For each impact parameter (velocity, angle, density, porosity, strength, and diameter), a quantile function

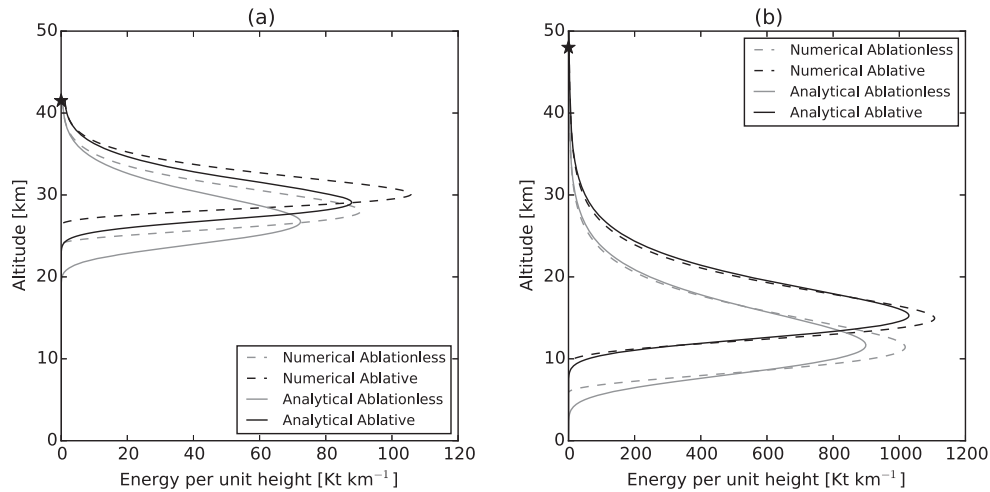


Fig. 1. Meteoroid kinetic energy loss per km as a function of altitude for a Chelyabinsk-scale airburst scenario (a) and a Tunguska-scale scenario (b). Shown are numerical solutions of the full pancake equations (dashed lines), both without (gray) and with (black) ablation, compared with the analytical approximation of Collins et al. (2005), which neglects ablation (solid gray), and the semianalytical approximation described here, which includes ablation (solid black). Models use the parameters in Table 1; stars indicate onset of pancaking at breakup altitude.

Table 1. Pancake model parameters.

Parameter	Chelyabinsk (0.55 Mt)	Tunguska (9.4 Mt)
Diameter [m]	19.5	50
Density [kg m^{-3}]	3300	3000
Velocity [km s^{-1}]	19	20
Angle [deg]	20	45
Strength [MPa]	2	1

Ablation parameter $K_H = 1.4 \times 10^{-8} \text{ kg J}^{-1}$; Drag coefficient $C_D = 2$; Atmosphere scale height $H = 8 \text{ km}$; Air density at surface $\rho_s = 1.22 \text{ kg m}^{-3}$.

was determined, relating the parameter to a probability between 0 and 1. For each airburst scenario, the impact parameters were selected randomly using these quantile functions and used in the ablative pancake model equations outlined in Appendix A. Figure 3 shows the frequency distributions for impactor velocity, angle, bulk density, and strength. The simulation output includes energy yield (taken to be the preimpact kinetic energy), burst height (altitude of peak kinetic energy loss to the atmosphere), and the residual kinetic energy at the burst altitude.

Impact Velocity

To define the velocity–frequency distribution of impacts on Earth, we use the model of Le Feuvre and Wiczorek (2011). Although impact speeds at the top of Earth’s atmosphere can range from escape velocity (11.2 km s^{-1}) to the maximum possible velocity (relative

to Earth) for an object orbiting the Sun at 1 AU (72 km s^{-1}), in almost all cases the entry speed is predicted to lie between 12 and 45 km s^{-1} , with a mean of 20.5 km s^{-1} (Le Feuvre and Wiczorek 2011). A piecewise power law provides a reasonable fit to the cumulative velocity–frequency distribution in the range $11\text{--}45 \text{ km s}^{-1}$ (Fig. 4). The corresponding quantile for impact velocity v_i is:

$$v_i = \begin{cases} 11 + 3.5 \left(\frac{P}{0.175} \right)^{0.593}, & P < 0.175 \\ 45 - 30.5 \left(\frac{1-P}{1-0.175} \right)^{0.443}, & P \geq 0.175 \end{cases} \quad [\text{kms}^{-1}] \quad (1)$$

Impact Angle

The mean angle of entry for an impactor is 45° to the target surface (Shoemaker 1962) and the relative probability is symmetrical around this point such that almost vertical and very shallow impacts are equally rare. The corresponding quantile function for the trajectory angle θ is:

$$\theta = \frac{\pi}{2} - \frac{1}{2} \cos^{-1}(2P - 1) \quad (2)$$

Density and Strength

Meteorite strength can be conveniently but crudely approximated as a function of density (Collins et al. 2005). However, for the few stony meteorite fragments that have undergone strength testing, the density measurements show

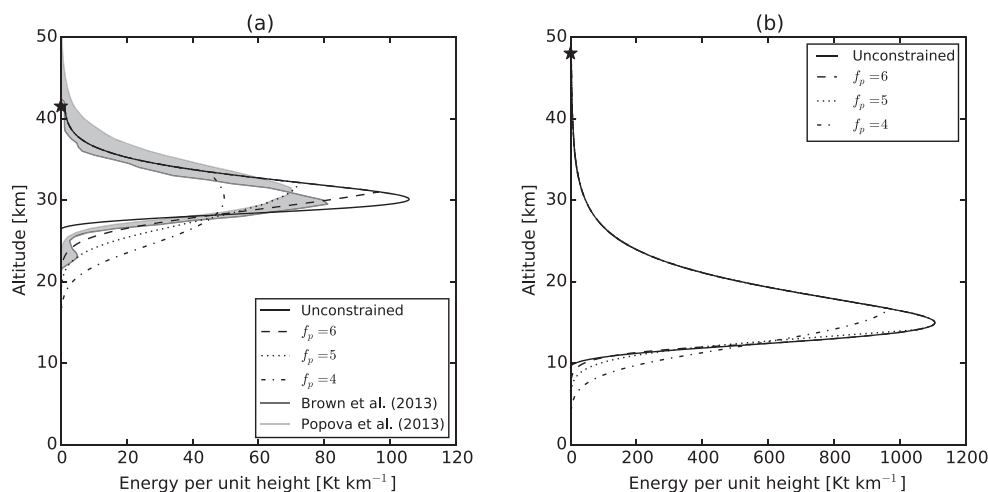


Fig. 2. Meteoroid kinetic energy loss per km as a function of altitude for a Chelyabinsk-scale airburst scenario (a) and a Tunguska-scale scenario (b). Shown are predictions of the pancake model with different constraints on the maximum pancake factor (f_p). Inferred energy deposition for the Chelyabinsk bolide based on light-curve data (Brown et al. 2013; Popova et al. 2013) are shown in (a) for comparison; the shaded region lies within the bounds of these two estimates. Models use the parameters in Table 1; stars indicate onset of pancaking at breakup altitude.

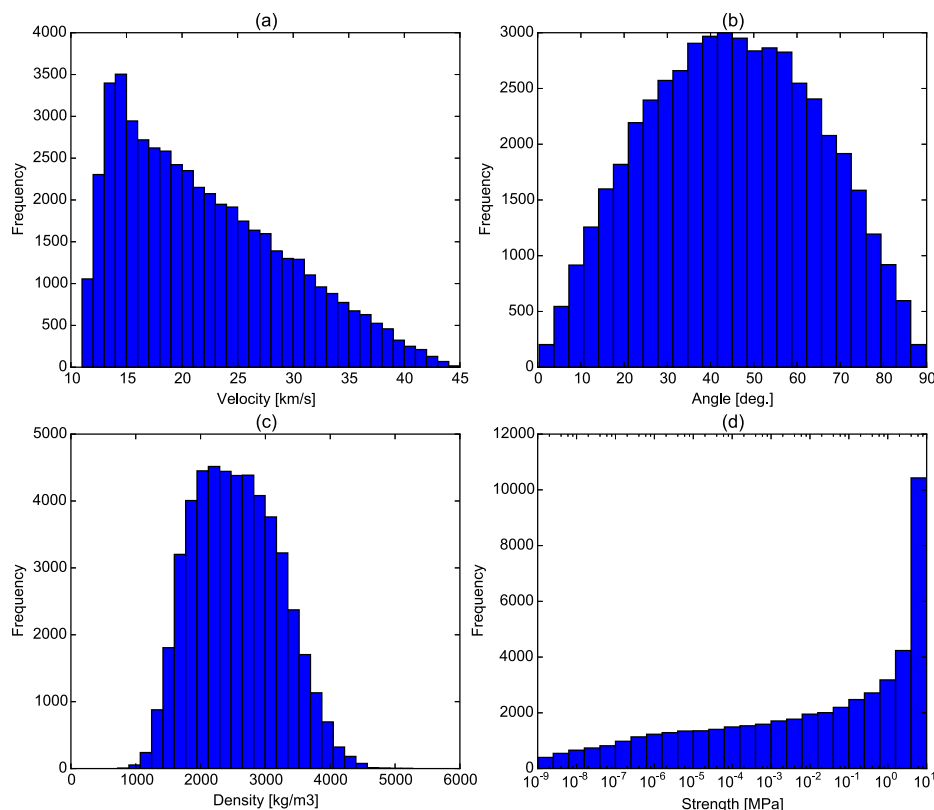


Fig. 3. Frequency distributions for the Monte Carlo simulation: (a) impactor speed; (b) impact trajectory angle to the target surface; (c) bulk impactor density; (d) impactor strength. (Color figure can be viewed at wileyonlinelibrary.com.)

moderate variation around a mean value (3490 kg m^{-3}), while tensile strengths vary over a two orders of magnitude from 1 to 100 MPa (Petrovic 2001).

In the absence of an obvious distribution among densities obtained from bolide-derived meteorite samples produced, we adopt a Gaussian probability frequency

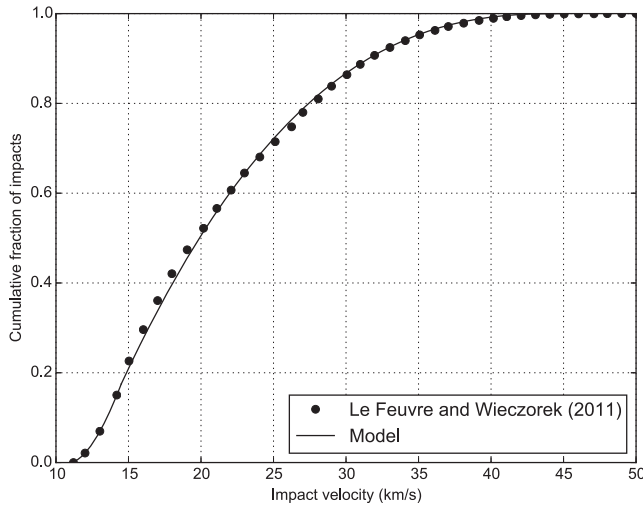


Fig. 4. Cumulative velocity–frequency distribution for Earth (Le Feuvre and Wieczorek 2011) and piecewise power law fit used to derive velocity quantile function for use in Monte Carlo simulation.

distribution centered about $\rho_{\text{avg}} = 3257 \text{ kg m}^{-3}$ with a standard deviation $\rho_{\text{std}} = 510 \text{ kg m}^{-3}$ (Medvedev et al. 1985; Borovička et al. 2003; Britt and Consolmagno 2003; Llorca et al. 2005; Hildebrand et al. 2006; Jenniskens et al. 2009; Kohout et al. 2011; Popova et al. 2011). The corresponding quantile function for the solid density of the impactor ρ_{si} is:

$$\rho_{\text{si}} = \rho_{\text{avg}} + \rho_{\text{std}} \sqrt{2} \text{erf}^{-1}(2P - 1) [\text{kg m}^{-3}] \quad (3)$$

This density represents the recovered meteorite sample density and accounts for variations in grain density and microporosity. As asteroids also exhibit a range of macroporosity from 0 to 50% (Britt et al. 2002), we calculate a bulk asteroid density by dividing ρ_{si} by a randomly selected distension $\alpha = (1 + P^2)$, which varies between 1 and 2, with a mean of 1.25 corresponding to a macroporosity of 20%.

The variation in asteroid strength has two parts. First, there is an underlying variation in the intrinsic tensile strength of meteorite fragments, which spans a range of 1–100 MPa (Petrovic 2001). In addition, there is an even larger variation in strength resulting from the natural, scale-dependent fracture distributions within asteroids (Popova et al. 2011). This variation is in part systematic: as rock mass increases so does the maximum flaw size, which is inversely correlated with tensile strength (Petrovic 2001). One way to account for this dependence of strength on size is to relate strength Y of an asteroid of mass m to the strength Y_0 of a meteorite sample of mass m_0 using a Weibull distribution (Weibull 1951):

$$Y = Y_0 \left(\frac{m_0}{m} \right)^\mu [\text{MPa}] \quad (4)$$

where the exponent μ determines the rate of strength reduction with mass. A wide range of Weibull exponents have been used to describe meteor strength in the past (see Popova et al. [2011] for a brief review). The most commonly used value is 0.25, based on the assumption that asteroids are relatively homogeneous materials (Tsvetkov and Skripnik 1991; Svetsov et al. 1995), though values between 0.1 and 0.75 encompass recent fireball data (Popova et al. 2011). As the variation in asteroid strength resulting from the choice of Weibull exponent is far greater than the range of measured meteorite tensile strengths, we adopt a nominal 1 kg mass tensile strength of $Y_0 = 10 \text{ MPa}$ ($m_0 = 1 \text{ kg}$) and randomly select the Weibull exponent using the quantile function: $\mu = P^2$, which gives a modal exponent of 0.25. For a 20 m diameter asteroid, this results in a modal strength of 0.2 MPa and a strength variation from $\sim 1 \text{ Pa}$ to 10 MPa.

Diameter

The impactor size-frequency distribution is a steep, negative power law function of impactor diameter L ; several million 10 m objects will enter Earth's atmosphere in the average time taken for one 160 m object to arrive (Brown et al. 2013). As our interest is the likelihood and variability of outcomes as a function of meteoroid size, rather than the precise probability of a given scenario, and because replicating steep distributions in a Monte Carlo simulation is computationally expensive, we instead use a simple distribution with $dN/dL \propto 1/L$. For equal log-diameter bin widths, this implies the same number of objects in each diameter bin. The quantile function of this distribution is given by:

$$\log L = \log L_{\min} + P(\log L_{\max} - \log L_{\min}) \quad (5)$$

where L_{\min} and L_{\max} are taken to be 5 and 160 m, respectively.

RESULTS

Monte Carlo modeling produced an artificial data set of $\sim 50,000$ airburst scenarios for stony asteroids in the size range 5–160 m (Fig. 5). The size of the data set was sufficient to achieve convergence in various quantiles of burst altitude as a function of energy (see below). In $\sim 2\%$ of scenarios the burst height was below the surface; these scenarios, which in reality would result in the asteroid impacting the ground at high

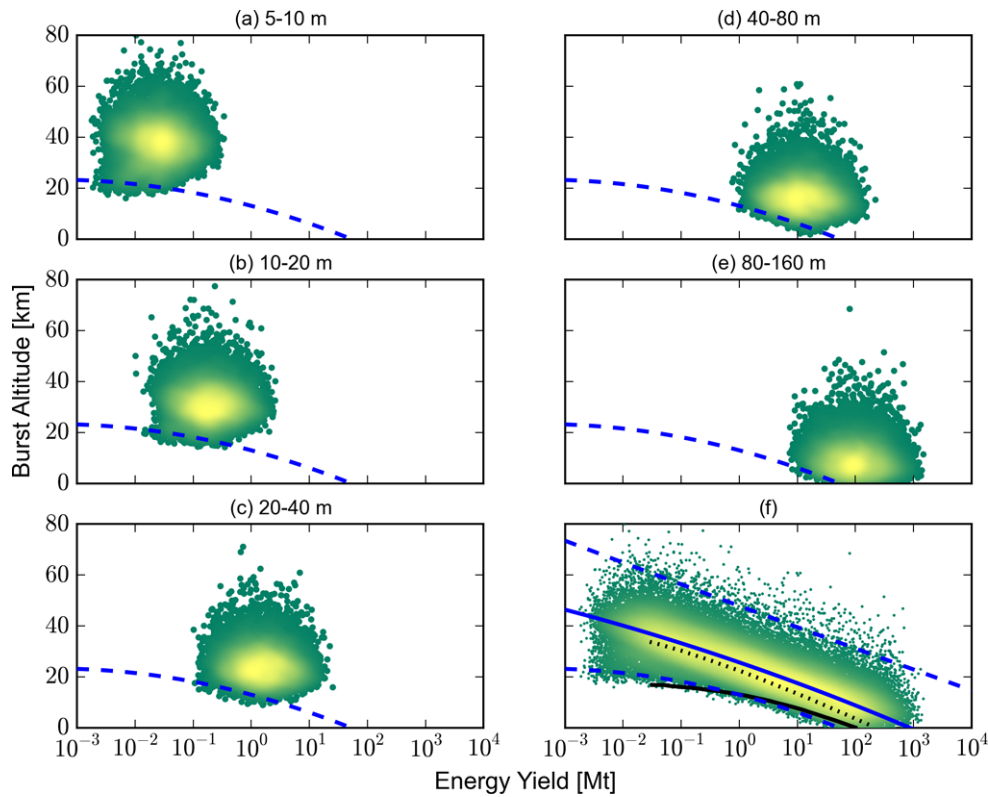


Fig. 5. Scatter plots of airburst scenarios in geometric diameter bins with a color scale representing point density (dark: minimum, light: maximum). Energy yield is taken as the kinetic energy of the impactor prior to atmospheric entry; the burst altitude is the altitude of peak kinetic energy loss to the atmosphere. Bottom-right: The complete artificial data set is plotted to display the spread of possible scenarios. The blue solid curve shows the median scenarios; the dotted lines show the 1st and 99th percentiles of the airburst scenarios. Also shown for comparison is the pancake model predictions of Toon et al. (1997) for stony (solid black line) and carbonaceous (dotted black line) asteroids. (Color figure can be viewed at wileyonlinelibrary.com.)

speed, are not shown in Fig. 5 but were used in the quantile regression. However, it is acknowledged that the transition from airburst to crater-forming scenarios is not discontinuous and there is an important intermediate regime where both airburst and cratering phenomena, and their interactions, are important (Shuvalov et al. 2013).

Separating the entire artificial data set into five bins of approximately equal number, with diameter bin widths (in m) of 5–10, 10–20, 20–40, 40–80, and 80–160, highlights the distribution in burst energy and altitude for scenarios with meteoroid diameters that differ by less than a factor of two. The two-to-three orders of magnitude variation in energy for each bin results primarily from variations in velocity, as well as mass (density and diameter); the spread in burst altitude is largely a consequence of the natural variation in density, strength, and impact angle, with weaker, low-density meteoroids on shallow trajectories favoring high-altitude disruption and vice versa. The point-density shading in Figs. 5a–e illustrates the relative likelihood of similar-diameter airburst scenarios.

The complete artificial airburst data set is shown in Fig. 5f. Note that the uniform distribution of scenarios in log-energy is a consequence of the artificial impactor size-frequency distribution used (Equation 5) to efficiently explore the effect of other variables. In reality, small energy scenarios are much more numerous than high-energy scenarios. The minimum burst altitude and modal burst altitude are well fit by second-order polynomials in $\log_{10} E_{Mt}$ where E_{Mt} is the pre-entry meteoroid energy in Mt. Hence, quantile regression using the Scipy statsmodels package (<http://statsmodels.sourceforge.net>) with a second-order polynomial fit was performed on data over the range $-1.5 < \log_{10} E_{Mt} < 2$. The resulting equations for the 1st, 50th, and 99th percentiles of burst altitude z_b (in km) are:

$$z_{b,1\%} = 13 - 6.04 \log_{10} E_{Mt} - 0.88 (\log_{10} E_{Mt})^2 \quad (6a)$$

$$z_{b,50\%} = 25.7 - 7.83 \log_{10} E_{Mt} - 0.31 (\log_{10} E_{Mt})^2 \quad (6b)$$

$$z_{b,99\%} = 47.9 - 8.43 \log_{10} E_{Mt} - 0.03 (\log_{10} E_{Mt})^2 \quad (6c)$$

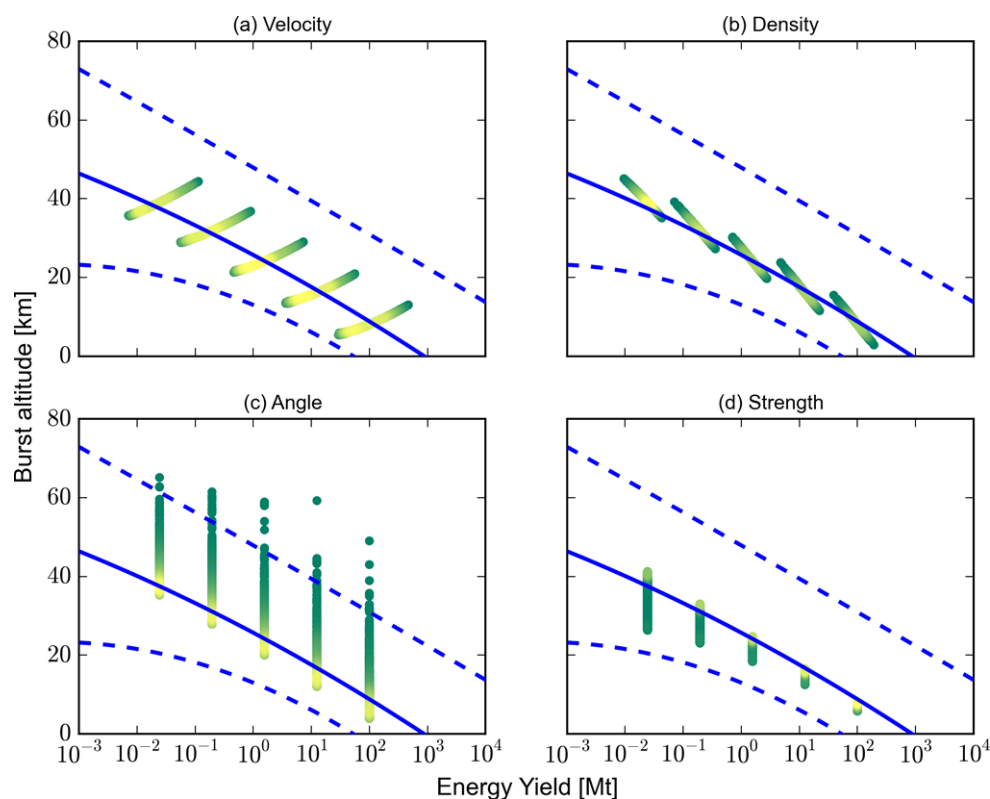


Fig. 6. Scatter plots of airburst scenarios for five impactor diameters (7, 14, 28, 56, and 113 m) showing the sensitivity of airburst altitude and energy to variation in individual impactor parameters: (a) impactor speed; (b) impactor density; (c) trajectory angle; and (d) impactor strength. The color scale represents point density (dark: minimum, light: maximum). Energy yield is taken as the kinetic energy of the impactor prior to atmospheric entry; the burst altitude is the altitude of peak kinetic energy loss to the atmosphere. The blue solid curve shows the median scenarios; the dotted lines show the 1st and 99th percentiles of the airburst scenarios. (Color figure can be viewed at wileyonlinelibrary.com.)

Equations 6a–c are also shown in Figs. 5 and 6 (blue lines); 98% of all airburst scenarios lie between $z_{b,1\%}$ and $z_{b,99\%}$ (dotted blue lines). The curve for $z_{b,1\%}$ can be considered a nominal “worst-case” scenario, which occurs at an altitude only 10–20 km below the median scenario for a given burst energy ($z_{b,50\%}$) depending on burst energy. Similarly, a nominal “best-case” scenario ($z_{b,99\%}$) occurs at an altitude ~ 23 km higher than the median scenario. Hence, the range of likely burst altitudes reduces with increasing airburst energy, although the range of asteroid strengths predicted by Equation 4 increases with asteroid size. This is because burst altitude is more sensitive to asteroid strength for small asteroid masses that decelerate at higher altitudes. For airbursts with energy exceeding a few Mt, deceleration occurs closer to the ground where aerodynamic stresses are much higher and disruption is less sensitive to asteroid strength.

The burst altitude of stony and carbonaceous asteroids as a function of energy predicted by Toon et al. (1997) are similar to our worst-case ($z_{b,1\%}$) and median ($z_{b,50\%}$) scenarios, respectively (black lines,

Fig. 5). This is because the (constant) strength and density Toon et al. used to represent stony asteroids are similar to the highest density and strength used in our Monte Carlo simulations (Equations 3 and 4), whereas the strength and density they assumed for carbonaceous asteroids is closer to the median strength and bulk density used here for stony asteroids with macroporosity. We note that our analysis excludes strong, dense iron asteroids and weak, low-density comets. While including these cases would extend the range of possible burst altitudes (Toon et al. 1997), their lower likelihood of occurrence implies that the statistical picture is likely to remain unchanged.

For Chelyabinsk-scale airbursts ($E_{Mt} \approx 0.5$), the median burst altitude from our analysis is 27.6 km, which is consistent with the 28–32 km range inferred from light-curve analysis (Fig. 2) (Brown et al. 2013; Popova et al. 2013). For Tunguska-scale airbursts ($E_{Mt} = 3$ –15), the median burst altitude is 21–15 km, somewhat higher than the inferred burst altitude of 5–15 km based on tree-fall geometry (Ben-Menahem 1975; Chyba et al. 1993; Svetsov 2007), suggesting that this

event was close to a worst-case scenario for its magnitude.

To illustrate the sensitivity of airburst altitude and energy to variation in the individual impactor parameters, we also performed four suites of Monte Carlo simulations that considered five specific impactor diameters, at the geometric center of each diameter bin (7, 14, 28, 56, and 113 m), and allowed only one impactor parameter to vary (Fig. 6). Impact angle has the greatest effect on burst altitude, whereas impact speed has the greatest effect on burst energy. Impact angle and strength only affect the burst altitude. Shallow-trajectory impacts define the “best-case” scenario, while strong impactors define the “worst-case” scenario. The effect of impact velocity, density, and angle is the same at all diameters. In contrast, the effect of strength is much more pronounced for small impactors; large airbursts are relatively insensitive to strength. The effects of impact speed on burst altitude and energy work in opposition: faster impactors burst higher in the atmosphere, but release more energy. The effects of density, on the other hand, work constructively: denser impactors burst lower and release more energy.

A NUMERICAL ASSESSMENT OF SIMPLE AIRBLAST MODELS USING ISALE

In addition to estimates of burst energy and burst altitude, fast estimation of airburst hazard requires a prescription for blastwave damage on the ground. In this section, we compare the widely employed static-source approximation for airburst blastwave damage to two alternative models that, while still simplified, attempt to account for the dynamic and directional nature of energy deposition in real meteoroid airbursts.

Approach

To simulate blastwaves formed by airbursts, we use the iSALE2D shock physics code (Wünnemann et al. 2006), a multimaterial, multirheology extension of the SALE hydrocode (Amsden et al. 1980). iSALE has been used extensively for the simulation of asteroid impacts on dense surfaces (Collins and Wünnemann 2005; Wünnemann et al. 2006; Davison and Collins 2007; Collins et al. 2008), but not the rather simpler application of shock propagation in a gas. We represent the (isothermal) atmosphere using a perfect gas equation of state in which pressure p is related to density ρ and specific internal energy E by $p = \Gamma \rho E$, with $\Gamma = 0.4$ and a reference density and pressure of 1 kg m^{-3} and 10^5 Pa at the base of the atmosphere. Three different approximations are used to represent energy deposition.

The first approach we consider is the static-source approximation, in which the meteoroid’s kinetic energy is converted to internal energy and deposited uniformly (and instantaneously) within a spherical region of the computational mesh, with a radius equal to an assumed “fireball” radius. The air density in the fireball is assumed to be the same as the ambient air. Based on exploratory simulations and observations from nuclear weapon tests (Glasstone and Dolan 1977, p. 70), we adopt a nominal fireball radius of 30–60 m for a 1 kt yield energy, which can be scaled to larger airburst energies by the cube-root of the energy in kt (see Discussion section). The second approach is a moving-source approximation. It is implemented in a manner similar to the static-source approach except that (1) the internal energy within the fireball is defined as the initial meteoroid kinetic energy minus the residual kinetic energy at the burst altitude and (2) the fireball is given an initial downward velocity, defined by the residual specific kinetic energy at the burst altitude. The assumption of vertically downward motion of the fireball is enforced by the cylindrical geometry of the two-dimensional model. The third and final approach, referred to here as the cylindrical line-source approximation, is to deposit the meteoroid’s energy along the vertical trajectory as a function of time based on the pancake model of disruption and deceleration. In this case, in each iSALE timestep, the kinetic energy transferred from the meteoroid to the atmosphere over the timestep duration is added as internal energy to a disk of cells, one cell high, at the altitude of the meteoroid and within a radius taken to be one-tenth the cylindrical equivalent blast radius, $R_b = (\frac{dE}{dz}/p_a)^{1/2}$, where p_a is the ambient atmospheric pressure (ReVelle 1976).

In each simulation, stationary probes were placed in every cell across the model surface to record peak air pressure as a function of distance from ground zero. Based on exploratory simulations, a spatial resolution of 10 cells across the source (fireball) radius was adopted as a compromise between accuracy and computational expense for the static- and moving-source simulations; an equivalent spatial resolution was used for the cylindrical line-source simulations. To verify the ability of the static-source approximation, as implemented in iSALE, to model atmospheric blastwaves, we compared results of static-source simulations with nuclear weapons test data for 1 kt explosions (Glasstone and Dolan 1977) and found good agreement.

RESULTS

We first compare our iSALE blastwave simulation results with the results of dynamic numerical airburst simulations using the SOVA hydrocode (Shuvalov et al. 2013). These simulations consider the blastwaves

produced by the atmospheric disruption of stony asteroids of diameters 20, 30, 40, and 50 m. In the static- and moving-source models, the fireball radius was set by yield scaling a nominal 1 kt fireball radius of 45 m, implying a specific internal energy of 8.968 MJ kg^{-1} . Ten computational cells resolved the fireball radius. Using the static-source approximation, the only free parameter is the altitude of burst (center of sphere of hot gas). We used altitudes of 21.8, 17, 13.5, and 10.9 km, which are approximately halfway between the worst-case ($z_{b,1\%}$) and median ($z_{b,50\%}$) scenarios from our Monte Carlo analysis, given by Equation 6. An additional free parameter in the moving-source approximation is the initial partitioning of fireball energy between internal and kinetic, which determines the energy density in the fireball and its initial downward velocity. Results from our Monte Carlo analysis showed that for a wide range of airburst parameters, the residual kinetic energy of the meteoroid at the burst altitude was tightly constrained to 0.33–0.34 times the initial kinetic energy (see also Appendix A). Hence, we adopted a constant kinetic energy partition of one-third for all moving-source simulations; the initial downward speed of the fireball is therefore given as the square-root of two-thirds of the specific energy of the fireball (2450 m s^{-1} in all scenarios considered here). As the cylindrical line-source approximation relies on the pancake model to determine energy deposition, it is dependent on several properties of the meteoroid. For the purpose of comparison with the SOVA results, we adopted the same meteoroid parameters as Shuvalov et al. (2013): speed (18 km s^{-1}), density (2650 kg m^{-3}), and a nominal low strength (0.2 MPa) for each airburst scenario. Impact angle was constrained to be vertical. In all simulations, an isothermal atmosphere with exponentially decreasing pressure and density was assumed.

The SOVA simulations that we compare to were performed in two steps: first, disruption, deformation, and evaporation of the asteroid was simulated in a reference frame following the asteroid; then, gas dynamic and thermodynamic parameters extracted from the first simulation were imposed as initial conditions for a second calculation in a larger domain that simulated the blastwave propagation and interaction with the ground surface (Shuvalov et al. 2013). In some ways, this approach is similar to our cylindrical line-source approximation, but with two important differences. First, in our approach, the pancake model is used to describe ablation and deformation of the asteroid, whereas Shuvalov et al. (2013) simulated asteroid ablation and deformation explicitly using SOVA. Second, our cylindrical line-source approximation deposits internal energy only, whereas

Shuvalov et al. (2013) used initial conditions that include air density and momentum, as well as internal energy. We note that radiative heat transfer is also included in SOVA, but not in iSALE and that SOVA uses a more realistic atmosphere equation of state.

A comparison of blastwave development using the three different energy deposition approximations for the 40 m airburst scenario is shown in Fig. 7. The static-source approximation results in a spherically propagating blastwave, emanating from the burst altitude (13.5 km in the 40 m scenario), with a sphere of rarefied air in its wake. The bottom row in Fig. 7 shows a moment shortly after the blast wave has reflected off the ground, forming a Mach stem (40 s in the 40 m scenario). The moving-source approximation results in similar phenomena; however, the downward momentum of the fireball produces a marked asymmetry in blastwave amplitude in the downward and upward directions, which results in a stronger blastwave amplitude at ground zero and an increased radius of the Mach stem at the times shown. The cylindrical line-source approximation produces a cylindrically expanding blastwave at altitudes above the peak energy deposition (burst) altitude. At lower altitudes, blastwave propagation is more spherical, but as less energy is released at low altitude, the spherical portion of the wave is considerably weaker than that in the static- and moving-source approximations. The amplitude of the blastwave vertically below the fireball is somewhat lower than that at azimuths more oblique to the fireball, owing to destructive interference of the shockwave emanating from different points along the meteoroids trajectory.

Figure 8 compares peak overpressure as a function of range for a 40 m asteroid airburst for the three different energy deposition approximations considered in this work and the simulation results from Shuvalov et al. (2013). At short ranges, close to ground zero, the moving source approximation is a good match to the results of the sophisticated SOVA calculation; both the static and cylindrical line-source approximations significantly underestimate the blastwave overpressure. However, at long ranges, the cylindrical line-source approximation appears to better match the SOVA simulation results. The more gradual decay of overpressure with range in the cylindrical line-source approximation is a consequence of the cylindrical (compared to spherical) geometry of the expanding blast wave. Similar results are observed for each asteroid size scenario.

Figure 9 shows the results of SOVA simulations for all four asteroid sizes compared to the corresponding moving-source approximation simulation using iSALE. In all cases, except for the 50 m asteroid scenario at

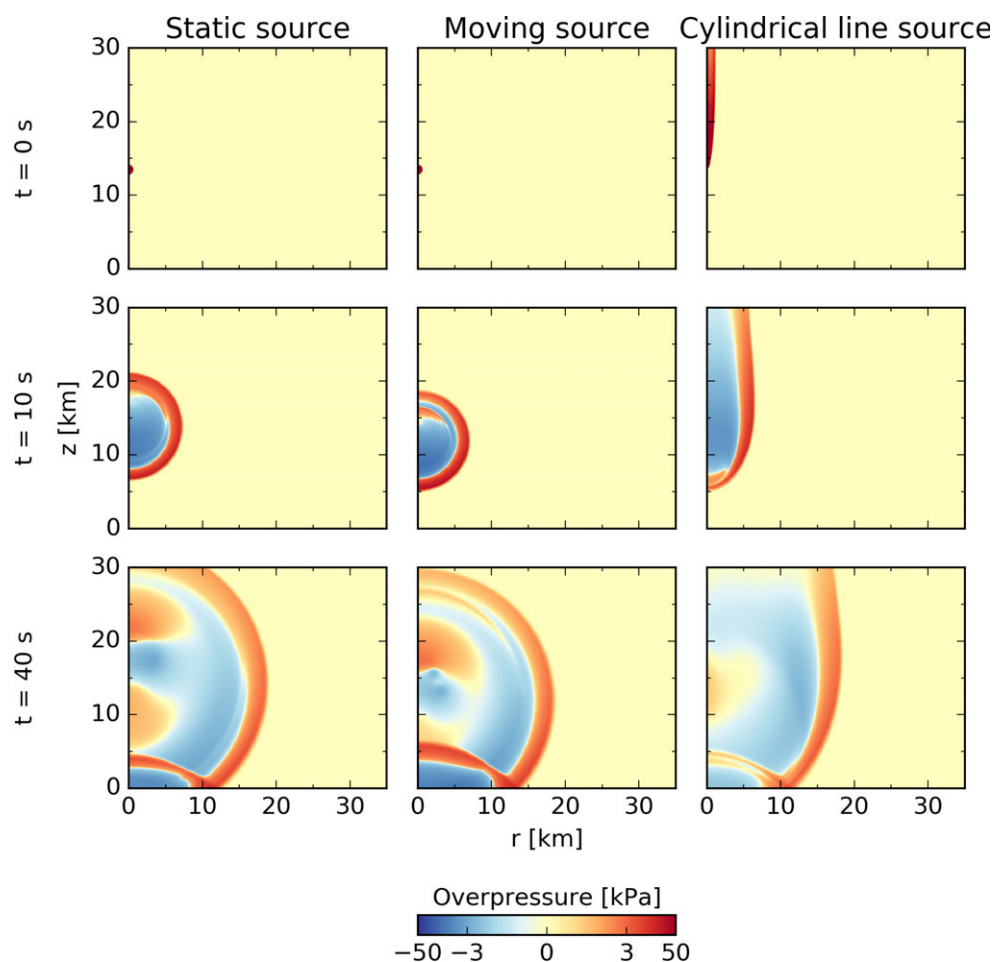


Fig. 7. Blastwave evolution for a 40 m diameter asteroid airburst at three discrete times after peak energy deposition from iSALE simulations using three different energy deposition approximations: stationary source, moving source, and cylindrical line source. Colors depict overpressure. (Color figure can be viewed at wileyonlinelibrary.com.)

peak overpressures exceeding 40 kPa, the iSALE results using the moving-source approximation are in excellent agreement with the SOVA simulation results. This suggests that the moving-source approximation offers an improvement for predicting blastwave damage in low-altitude (subvertical) airbursts compared to the static-source approximation. We note that the results of the moving-source model are dependent on the choice of initial fireball velocity, which in turn depends on the assumed fireball mass and residual kinetic energy at burst. However, the good agreement between the moving-source model adopted here and the SOVA simulation results suggests our rationale for determining the fireball speed is reasonable.

In addition to the comparison with SOVA results, we also applied the three simple airblast modeling approaches to four hypothetical scenarios with different burst energies: 0.5 Mt (approximately the scale of the Chelyabinsk airburst), 5 Mt and 15 Mt (lower and upper estimates for Tunguska), and 50 Mt. We

emphasize that the purpose of this exercise was not to accurately reproduce historical events, which requires more sophisticated 3D numerical modeling and has been demonstrated previously (e.g., Popova et al. 2013; Avramenko et al. 2014; Aftosmis et al. 2016). Rather, our purpose was to quantify the approximate differences in blast wave magnitude for a range of airburst energies according to the three different approximations, which can be regarded as a measure of uncertainty when applying simple protocols for blast damage estimation. The model set-up for these simulations was the same as for the SOVA comparisons, with the following exceptions. In the static- and moving-source models, we used initial burst altitudes of 21.5, 14, 10, and 11 km, respectively, for the different energy scenarios. For the three lowest energy scenarios, these burst altitudes are between the worst-case ($z_{b,1\%}$) and median ($z_{b,50\%}$) scenarios from our Monte Carlo analysis, given by Equation 6. For the 50 Mt scenario, the burst altitude was set to the median

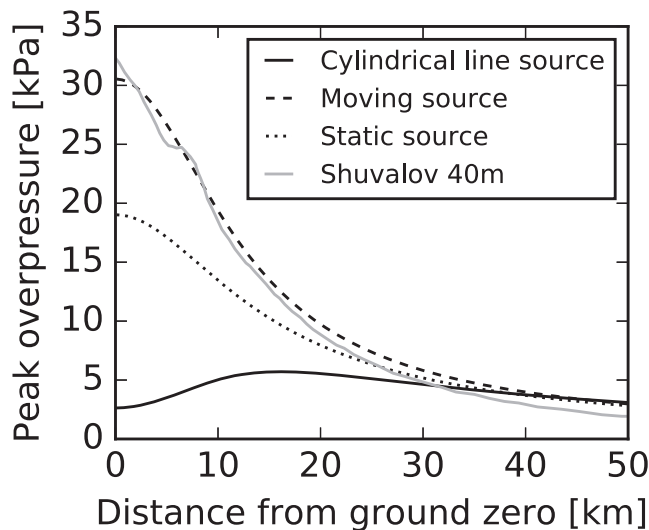


Fig. 8. Peak overpressure as a function of range for a 40 m asteroid airburst for the three different energy deposition approximations considered in this work and the simulation results from Shuvalov et al. (2013). The static-source approximation assumes a burst altitude of 13.5 km. The moving-source approximation further assumes an initial downward speed of 2450 m s^{-1} for the fireball, based on the assumption that the residual kinetic energy of the meteor at burst is one-third the initial kinetic energy. The cylindrical line-source approximation assumes a time-dependent energy deposition derived from the pancake model, with meteoroid parameters: $L = 40$; $v_i = 18 \text{ m s}^{-1}$; $\rho = 2650 \text{ g m}^{-3}$; $Y = 0.2 \text{ Pa}$.

burst altitude, because in the worst-case scenario the meteoroid strikes the ground. In the cylindrical line-source model, we considered only one representative scenario of fixed meteoroid diameter, speed (20 km s^{-1}), density (3000 kg m^{-3}), and strength (0.2 MPa) for each airburst energy scale.

The results of our simple airburst blastwave models are presented in Table 2. Documented are the peak pressure at ground zero and the pressure at a range equivalent to three times the burst altitude. Also recorded were the range at which several overpressure values were observed: 1 kPa (approximate overpressure for window damage), 10 kPa, 20 kPa (lower and upper limits for extensive tree damage), and 35 kPa (brick building damage). In each of the different energy deposition scenarios, the peak overpressures predicted by all three energy deposition approximations are in good agreement at (and beyond) a range of three times the burst altitude. However, at ground zero, the three different approximations show a large variation in peak overpressure. The static-source approximation is consistently intermediate between the moving-source approximation and the cylindrical line-source approximation. The moving-source approximation predicts overpressures approximately up to twice the size of the static-source approximation. The cylindrical

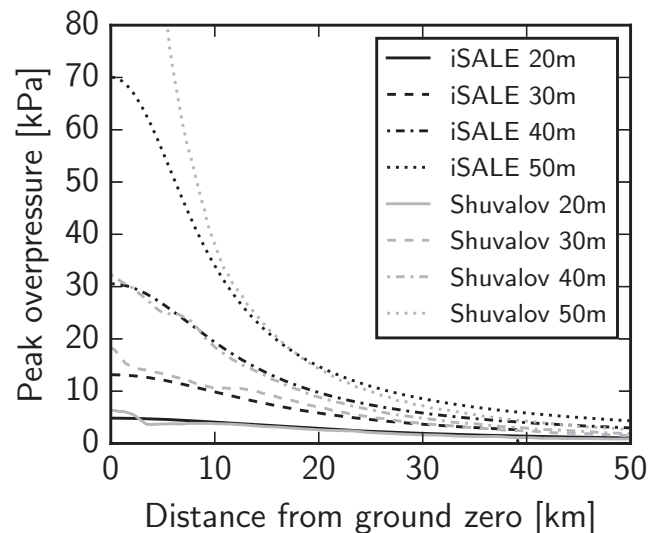


Fig. 9. Peak overpressure as a function of range for four airburst scenarios of different asteroid diameters comparing results from the moving-source approximation and simulation results of Shuvalov et al. (2013). In the four iSALE simulations the assumed burst altitudes were 21.8, 17, 13.5, and 10.9 km, respectively, and the downward fireball speeds were of 2450 m s^{-1} for the fireball, based on the assumption that the residual kinetic energy of the meteor at burst is one-third the initial kinetic energy.

line-source approximation predicts overpressures 2–4 times lower than the static-source approximation depending on the airburst energy.

The ~500 kt Chelyabinsk airburst caused minor building damage and broken windows over an elliptical area of $\sim 10,000 \text{ km}^2$ elongated in the direction transverse to the fireball trajectory (Popova et al. 2013). This extent of blast damage is very consistent with 3D numerical simulations of blastwave propagation using an energy deposition model similar to the cylindrical line-source approach employed here (Avramenko et al. 2014; Aftosmis et al. 2016). The simplified models documented in Table 2 assumed a vertical (or no) trajectory, implying symmetric, circular blast damage contours; however, it is instructive to compare the predicted extent of blast damage with observations and more sophisticated models. Assuming window damage requires an overpressure $\sim 1 \text{ kPa}$ (0.5–5 kPa, Glasstone and Dolan 1977, p. 221; Popova et al. 2013), all three energy deposition approximations predict a $\sim 50 \text{ km}$ radius damage zone, which is broadly consistent with observations (Brown et al. 2013; Popova et al. 2013). At this high burst altitude, there is less difference between the moving-source and static-source approximations than for larger, lower airbursts. Although the cylindrical line-source model predicts lower peak overpressures close to ground zero, beyond $\sim 60 \text{ km}$ range peak overpressures are greater for the cylindrical line source

Table 2. Blastwave outcomes from airburst simulations.

Airburst energy (Mt)	Peak overpressure (kPa)			Overpressure at $r = 3z_b$ (kPa)			1 kPa range (km)			10 kPa range (km)			20 kPa range (km)			35 kPa range (km)		
	S	M	C	S	M	C	S	M	C	S	M	C	S	M	C	S	M	C
0.5	3.81	5.27	1.32	0.786	0.811	0.894	52.3	54.8	55.5	n/a	n/a	n/a	n/a	n/a	n/a	n/a	n/a	n/a
5	21.6	35.2	7.56	4.16	4.41	4.37	142	140	—	18.7	22.4	n/a	4.48	11.8	n/a	n/a	1.16	n/a
15	65.8	143	26.5	11.8	13.0	12.2	257	236	—	34.4	36.2	37.0	19.2	22.1	16.0	11.1	14.9	n/a
50	116	326	35.7	19.6	20.5	15.5	—	—	—	57.0	54.3	52.9	32.4	33.5	24.0	20.4	23.3	4.23

S, static source; M, moving source; C, cylindrical line source.

n/a: No overpressure of this magnitude is reached in the simulation.

—: This overpressure is too low to be observed in the computational mesh.

than the two spherical sources, owing to the shallower attenuation of cylindrical waves with propagation distance compared to spherical waves, consistent with the results of 3D simulations of the Chelyabinsk airblast (Aftosmis et al. 2016). For shallow trajectories, this will imply strongly asymmetric blast contours. It seems clear that high-altitude, shallow-trajectory airbursts, such as Chelyabinsk, are best modeled by a cylindrical line-source approach and hence require a 3D shock physics calculation. Nevertheless, even in this case, the static-source approximation serves as a useful first-order approximation.

Recent estimates of the Tunguska airburst energy yield vary from ~3–5 Mt (Boslough and Crawford 2008) to 10–20 Mt (Artemieva and Shuvalov 2007, 2016). The ~2200 km² areal extent of treefall suggests wind speeds >40 m s⁻¹ and overpressures >20 kPa extended to a radius ~25 km from the blast epicenter according to nominal blastwave effects (Glasstone and Dolan 1977); however, these may represent conservative thresholds by a factor of two, as local topographic effects and poor tree condition may have exacerbated the tree damage (Boslough and Crawford 2008).

Two of the airburst scenarios we considered can be compared with the Tunguska event: 5 Mt and 15 Mt. In the smaller energy scenario, the static-source and, in particular, the moving-source approximations are approximately consistent with observations, provided that blastwave amplification by topography and poor tree health are invoked. In this case, peak overpressures of >10 kPa and wind speeds of >20 m s⁻¹ extend to a radius of 18–22 km. In the 5 Mt scenario, the cylindrical line-source approximation does not predict conditions required for extensive tree damage, even allowing for a factor of two reduction in the pressure and wind speed thresholds. In the 15 Mt scenario, the nominal conditions for extensive tree damage (40 m s⁻¹ winds; 20 kPa over pressure) are achieved to a radial distance of 16–22 km for all of the source approximations, with the (vertical) cylindrical line-source approximation providing the most conservative prediction of damage extent and the moving source approximation providing the worst-case estimate.

Another useful metric for blast damage is the overpressure required to completely destroy brick walls (35 kPa, Glasstone and Dolan 1977, p. 182; Collins et al. 2005). In the 5 Mt scenario, this level of peak overpressure is barely reached at ground zero even according to the least-conservative, moving-source approximation; in the 15 Mt scenario, extensive building damage is expected to a range of 10–15 km according to the moving-source and static-source approximations, but is not expected according to the cylindrical line-source approximation.

The largest energy case we consider is a 50 Mt airburst at 11 km nominal burst altitude. This is the same yield energy as the Tsar nuclear bomb test and represents an approximate estimate of the typical (modal) airburst scenario at the threshold of forming an impact crater (Fig. 5). In this case, extensive building damage is expected to a range of 20–23 km, according to both the moving-source and static-source approximations. Clearly, an airburst of this magnitude over a heavily populated urban area would be devastating. The peak overpressures predicted by the cylindrical line-source approximation are again much less than the spherical source approximations within a range equivalent to three times the burst altitude (33 km). For scenarios of the same energy but lower burst altitudes this would be exacerbated by the fact that in such cases the pancake model predicts the meteoroid still possesses significant kinetic energy upon reaching the ground. Any contribution of this energy to atmospheric disturbance would be neglected in a simple application of the cylindrical line-source model. However, the residual kinetic energy of the impactor would be expended modifying the ground and ejecting debris into the atmosphere at high speeds. A much more sophisticated shock physics calculation is required to determine the outcome in such cases (Shuvalov et al. 2013).

DISCUSSION

Based on CTH simulation results of low-altitude airbursts, Boslough and Crawford (2008) concluded that the altitude of maximum energy deposition is not a good estimate of the equivalent height of a static-source explosion and suggested that the residual downward speed of the meteoroid at burst needed to be taken into account in airburst damage assessment. Our results support this conclusion and show that a relatively simple method to account for the residual speed is to give the spherical source region an initial downward velocity under the assumption of 2:1 internal-to-kinetic energy partitioning at burst, which is a robust prediction of our Monte Carlo pancake model airburst simulation.

Probabilistic hazard assessments for asteroid impacts (Reinhardt et al. 2016) require hundreds of thousands of impact scenarios to be computed to derive robust statistics. In this case, the efficiency of blastwave damage estimation is paramount and high accuracy is secondary. The 2D shock physics calculations in this work each took approximately 48 h on a single CPU on a standard computer workstation. Even with the additional efficiency of parallel processing, such calculations are impractical if large numbers of scenarios need to be considered, particularly if 3D calculations are required.

Given the success of the moving-source approximation in our work, it may be fruitful to explore an analytical approach to modify the static-source blastwave scaling laws (Collins et al. 2005) to account for advection of the source. In the meantime, as the moving-source (and cylindrical line-source) approach requires a shock physics calculation and appears to consistently predict overpressures approximately two times larger than the static-source approximation, a more simplistic, but computationally expedient approach for the purposes of probabilistic hazard assessment is to retain the static-source methodology, but incorporate the factor of two amplification of overpressure inside a range of three times the burst altitude as a correction or measure of uncertainty.

In the subvertical airburst scenarios that we considered, the cylindrical line-source approximation underestimates the severity of blast damage near ground zero, even though it is based on a more faithful along-trajectory deposition of energy than the static-source approximation, which deposits all the airburst energy in a small spherical volume. This is consistent with results of 3D simulations of vertical airbursts that also compared the static-source and line-source approaches (Aftosmis et al. 2016). It is likely that the deficiency of the line-source approach is because it neglects the momentum of the air imparted by the decelerating meteoroid. SOVA simulations that impose along-trajectory consequences of meteoroid disruption that include internal energy and gas velocity as initial conditions in airblast propagation simulations produce much stronger blastwaves near ground zero (Shuvalov et al. 2013). Future work should consider modifications to the cylindrical line-source approach to incorporate fireball momentum, perhaps by inferring along-trajectory gas dynamics from the pancake model and coupling this information to the shock physics calculation in tandem with internal energy deposition. However, we note that 3D simulations of the Chelyabinsk airburst using the line-source approach have been very successful in replicating blast damage on the ground (Popova et al. 2013; Avramenko et al. 2014; Aftosmis et al. 2016). Hence, it is likely that the cylindrical line-source approximation is the best approach for modeling high-altitude, shallow-trajectory airbursts. An important strength of the cylindrical line-source approximation that is not apparent in our vertical-trajectory simulations is that for oblique trajectories, it produces asymmetric blast damage contours on the ground, consistent with observations (Popova et al. 2013). Indeed, for very shallow-angle trajectories, the cylindrical line-source approximation would likely predict higher overpressures at ground zero (directly beneath the point of peak energy deposition) than the spherical source approximations,

because of the less rapid attenuation of cylindrically expanding (compared with spherically expanding) waves.

The Earth Impact Effects Program (impact.ese.ic.ac.uk) is an online resource for quickly estimating the consequences of asteroid impacts on Earth (Collins et al. 2005), suitable for probabilistic hazard assessment (Reinhardt et al. 2016). To estimate blastwave damage, the program uses a combination of an analytical approximation to the pancake model (Collins et al. 2005), yield scaling, and measured blastwave attenuation in nuclear weapons tests at various altitudes (Glasstone and Dolan 1977). Shuvalov et al. (2013) showed that the web program's predictions are in reasonable agreement with sophisticated shock physics calculations of airburst blastwaves aside from near the transition from airburst-forming to crater-forming impacts. In addition, the original version of the web program also underestimates the overpressure at ground zero for Chelyabinsk-scale airbursts by an order of magnitude. Here we describe three improvements to the web program to address these deficiencies and to incorporate the new insight from our airburst simulations.

To better account for blastwave effects in events transitional between airbursts and crater-forming impacts, the program is modified to use the maximum of the residual kinetic energy of the meteoroid at the ground (i.e., impact energy) and the total kinetic energy transferred to the atmosphere at the burst altitude as the airburst energy for use in the static-source airblast approximation. Previously, the calculator used the former for all crater-forming scenarios, thereby neglecting large atmospheric energy deposition in small crater-forming impacts. In addition, we found that the procedure described in Collins et al. (2005) for relating peak overpressure $p(r)$ (Pa) at range r (m) to burst altitude z_b (m) for 1 kt explosions (Equations 55 and 56) overestimates the attenuation of the blastwave with distance for high-altitude bursts. A better fit to the nuclear test data (Glasstone and Dolan 1977) over a greater altitude range is given by the single expression:

$$p(r) = 3.14 \times 10^{11} (r^2 + z_b^2)^{-2.6/2} + 1.8 \times 10^7 (r^2 + z_b^2)^{-1.13/2} \quad (7)$$

With this modification, the peak overpressure at ground zero ($r = 0$) for a Chelyabinsk-scale airburst increases from ~ 0.1 to ~ 1 kPa, in much better agreement with observation. Finally, to incorporate the conclusions of this work, the web program is modified to report a factor of two range of overpressures within a range equal to three times the burst altitude, with the lower limit of this range estimated from the static-source approximation.

CONCLUSIONS

Using numerical modeling, we have re-examined the static-source approximation as a procedure for estimating airburst blast damage. A Monte Carlo model of stony asteroid airbursts that uses a fast, semianalytical approximation of the pancake model of a meteoroid's atmospheric disruption and ablation and accounts for natural variation in meteoroid speed, density, trajectory angle, and strength, shows that for a given burst energy, 98% of airburst scenarios occur within a ~ 35 km range in altitude and that half of these occur in the lowest ~ 12 km of this range. Hence, the majority of airburst scenarios occur at altitudes not much higher than the worst-case scenario. According to our analysis, the Tunguska airburst was probably close to a worst-case scenario for its energy. The Chelyabinsk airburst, on the other hand, occurred at an altitude several kilometers above the worst-case scenario for its size range, primarily because of the shallow angle of the meteoroid's trajectory. The energy deposition per unit path length of both of these stony asteroid airburst events is well described by the ablative pancake model, despite its simplicity and unphysical predictions of meteoroid geometry at burst.

The iSALE 2D shock physics code was used to simulate blastwave formation, attenuation, and interaction with the surface under three energy deposition approximations: a spherical static source of internal energy equivalent to the impact energy, a spherical moving source with a one-third kinetic-to-internal energy partitioning, and a cylindrical line source with the energy per unit path length determined by the pancake model. The three simple approaches applied to vertical impact airbursts produce consistent blastwave amplitude estimates beyond a range equivalent to approximately three times the burst altitude; inside this range, they disagree by almost an order of magnitude. The moving-source model, which provides the best match to detailed hydrodynamic simulation of meteoroid disruption in the atmosphere (Shuvalov et al. 2013), predicts the greatest blastwave amplitude at ground zero, approximately two times larger than that predicted by the static-source approximation. The cylindrical line-source approximation predicts blast amplitudes at ground zero several times smaller than the static-source approximation, but owing to the cylindrical expansion of the blastwaves, these amplitudes attenuate less rapidly with distance than the spherically expanding wave from the static source.

For fast estimation of airblast effects, suitable for hazard assessment, our work suggests that the static-source approach provides a reasonable first-order approximation of blastwave damage, but may

underestimate overpressures by a factor of two near ground zero. Incorporating this correction or uncertainty into the simple, static-approximation scaling laws is a much more expedient approach than performing shock physics calculations. However, for a more accurate estimate of blast wave effects, or if more time is available to assess the hazard, the moving-source approximation appears to provide the best simple approach for approximating low-altitude airbursts, particularly for subvertical trajectories. For high-altitude or shallow-trajectory airbursts, the cylindrical line-source approximation is likely to be the best simple approach, although more work is required to determine the optimum approach for coupling the pancake model to a shock physics code.

Acknowledgments—We thank two anonymous reviewers and Natasha Artemieva for their constructive comments that improved this paper. We gratefully acknowledge the developers of iSALE (www.isale-code.de). GSC and TMD acknowledge funding from STFC grant: ST/N000803/1.

Editorial Handling—Dr. Natalia Artemieva

REFERENCES

- Aftosmis M. J., Nemec M., Mathias D., and Berger M. 2016. Numerical simulation of bolide entry with ground footprint prediction. In *54th AIAA aerospace sciences meeting*. American Institute of Aeronautics and Astronautics. <http://arc.aiaa.org/doi/10.2514/6.2016-0998>. Accessed December 14, 2016.
- Amsden A. A., Ruppel H. M., and Hirt C. W. 1980. *SALE: Simplified ALE computer program for fluid flow at all speeds*. Los Alamos, New Mexico: Los Alamos National Laboratory. p. 101.
- Artemieva N. and Pierazzo E. 2009. The Canyon Diablo impact event: Projectile motion through the atmosphere. *Meteoritics & Planetary Science* 44:25–42.
- Artemieva N. A. and Shuvalov V. V. 2001. Motion of a fragmented meteoroid through the planetary atmosphere. *Journal of Geophysical Research: Planets* 106:3297–3309.
- Artemieva N. and Shuvalov V. 2007. 3D effects of Tunguska event on the ground and in atmosphere (abstract #1537). 38th Lunar and Planetary Institute Science Conference. CD-ROM.
- Artemieva N. A. and Shuvalov V. V. 2016. From Tunguska to Chelyabinsk via Jupiter. *Annual Review of Earth and Planetary Sciences* 44:37–56.
- Avramenko M. I., Glazyrin I. V., Ionov G. V., and Karpeev A. V. 2014. Simulation of the airwave caused by the Chelyabinsk superbolide. *Journal of Geophysical Research: Atmospheres* 119:2013JD021028.
- Ben-Menahem A. 1975. Source parameters of the Siberian explosion of June 30, 1908, from analysis and synthesis of seismic signals at four stations. *Physics of the Earth and Planetary Interiors* 11:1–35.
- Borovička J., Weber H. W., Jopek T., Jakeš P., Randa Z., Brown P. G., Revelle D. O., Kalenda P., Schultz L., Kucera J., Haloda J., Týcová P., Frýda J., and Brandstätter F. 2003. The Morávka meteorite fall: 3. Meteoroid initial size, history, structure, and composition. *Meteoritics & Planetary Science* 38:1005–1021.
- Boslough M. B. E. and Crawford D. A. 2008. Low-altitude airbursts and the impact threat. *International Journal of Impact Engineering* 35:1441–1448.
- Britt D. T. and Consolmagno G. J. S. J. 2003. Stony meteorite porosities and densities: A review of the data through 2001. *Meteoritics & Planetary Science* 38:1161–1180.
- Britt D. T., Yeomans D., Housen K., and Consolmagno G. 2002. Asteroid density, porosity, and structure. In *Asteroids III*, edited by Bottke W. F. Jr., Cellino A., Paolicchi P., and Binzel R. P. Tucson, Arizona: University of Arizona Press, pp. 485–500.
- Brown P. G., Assink J. D., Astiz L., Blaauw R., Boslough M. B., Borovička J., Brachet N., Brown D., Campbell-Brown M., Ceranna L., Cooke W., de Groot-Hedlin C., Drob D. P., Edwards W., Evers L. G., Garces M., Gill J., Hedlin M., Kingery A., Laske G., Le Pichon A., Mialle P., Moser D. E., Saffer A., Silber E., Smets P., Spalding R. E., Spurný P., Tagliaferri E., Uren D., Weryk R. J., Whitaker R., and Krzeminski Z. 2013. A 500-kiloton airburst over Chelyabinsk and an enhanced hazard from small impactors. *Nature* 503:238–241.
- Chyba C. F., Thomas P. J., and Zahnle K. J. 1993. The 1908 Tunguska explosion: Atmospheric disruption of a stony asteroid. *Nature* 361:40–44.
- Collins G. S. and Wünnemann K. 2005. How big was the Chesapeake Bay impact? Insight from numerical modeling. *Geology* 33:925–928.
- Collins G. S., Melosh H. J., and Marcus R. A. 2005. Earth Impact Effects Program: A Web-based computer program for calculating the regional environmental consequences of a meteoroid impact on Earth. *Meteoritics & Planetary Science* 40:817–840.
- Collins G. S., Kenkmann T., Osinski G. R., and Wünnemann K. 2008. Mid-sized complex crater formation in mixed crystalline-sedimentary targets: Insight from modeling and observation. *Meteoritics & Planetary Science* 43:1955–1977.
- Davison T. and Collins G. S. 2007. The effect of the oceans on the terrestrial crater size-frequency distribution: Insight from numerical modeling. *Meteoritics & Planetary Science* 42:1915–1927.
- Glasstone S. and Dolan P. J. 1977. *The effects of nuclear weapons*, 3rd ed. Washington, D.C.: Department of Defense and Energy. 653 p.
- Hildebrand A. R., McCausland P. J. A., Brown P. G., Longstaffe F. J., Russell S. D. J., Tagliaferri E., Wacker J. F., and Mazur M. J. 2006. The fall and recovery of the Tagish Lake meteorite. *Meteoritics & Planetary Science* 41:407–431.
- Hills J. G. and Goda M. P. 1993. The fragmentation of small asteroids in the atmosphere. *The Astronomical Journal* 105:1114–1144.
- Jenniskens P., Shaddad M. H., Numan D., Elsir S., Kudoda A. M., Zolensky M. E., Le L., Robinson G. A., Friedrich J. M., Rumble D., Steele A., Chesley S. R., Fitzsimmons A., Duddy S., Hsieh H. H., Ramsay G., Brown P. G., Edwards W. N., Tagliaferri E., Boslough M. B., Spalding R. E., Dantowitz R., Kozubal M., Pravec P., Borovička J., Charvat Z., Vaubaillon J., Kuiper J., Albers J., Bishop

- J. L., Mancinelli R. L., Sandford S. A., Milam S. N., Nuevo M., and Worden S. P. 2009. The impact and recovery of asteroid 2008 TC₃. *Nature* 458:485–488.
- Kohout T., Kiuru R., Montonen M., Scheirich P., Britt D., Macke R., and Consolmagno G. 2011. Internal structure and physical properties of the Asteroid 2008 TC3 inferred from a study of the Almahata Sitta meteorites. *Icarus* 212:697–700.
- Le Feuvre M. and Wieczorek M. A. 2011. Nonuniform cratering of the Moon and a revised crater chronology of the inner solar system. *Icarus* 214:1–20.
- Llorca J., Trigo-Rodríguez J. M., Ortiz J. L., Docobo J. A., García-Guinea J., Castro-Tirado A. J., Rubin A. E., Eugster O., Edwards W., Laubenstein M., and Casanova I. 2005. The Villalbeto de la Peña meteorite fall: I. Fireball energy, meteorite recovery, strewn field, and petrography. *Meteoritics & Planetary Science* 40:795–804.
- Medvedev R. V., Gorbachevich F. I., and Zotkin I. T. 1985. Determination of the physical properties of stony meteorites with application to the study of processes of their destruction. *Meteoritika* 44:105–110.
- Passey Q. R. and Melosh H. J. 1980. Effects of atmospheric breakup on crater field formation. *Icarus* 42:211–233.
- Petrovic J. J. 2001. Review: Mechanical properties of meteorites and their constituents. *Journal of Materials Science* 36:1579–1583.
- Popova O., Borovička J., Hartmann W. K., Spurný P., Gnos E., Nemtchinov I., and Trigo-Rodríguez J. M. 2011. Very low strengths of interplanetary meteoroids and small asteroids. *Meteoritics & Planetary Science* 46:1525–1550.
- Popova O. P., Jenniskens P., Emel'yanenko V., Kartashova A., Biryukov E., Khaibrakhmanov S., Shuvalov V., Rybnov Y., Dudorov A., Grokhovsky V. I., Badyukov D. D., Yin Q. Z., Gural P. S., Albers J., Granvik M., Evers L. G., Kuiper J., Kharlamov V., Solovyov A., Rusakov Y. S., Korotkiy S., Serdyuk I., Korochantsev A. V., Larionov M. Y., Glazachev D., Mayer A. E., Gisler G., Gladkovsky S. V., Wimpenny J., Sanborn M. E., Yamakawa A., Verosub K. L., Rowland D. J., Roeske S., Botto N. W., Friedrich J. M., Zolensky M. E., Le L., Ross D., Ziegler K., Nakamura T., Ahn I., Lee J. I., Zhou Q., Li X. H., Li Q. L., Liu Y., Tang G. Q., Hiroi T., Sears D., Weinstein I. A., Vokhmintsev A. S., Ishchenko A. V., Schmitt-Kopplin P., Hertkorn N., Nagao K., Haba M. K., Komatsu M., and Mikouchi T.; Chelyabinsk Airburst Consortium. 2013. Chelyabinsk airburst, damage assessment, meteorite recovery, and characterization. *Science* 342:1069–1073.
- Reinhardt J. C., Chen X., Liu W., Manchev P., and Paté-Cornell M. E. 2016. Asteroid risk assessment: A probabilistic approach. *Risk Analysis* 36:244–261.
- ReVelle D. O. 1976. On meteor-generated infrasound. *Journal of Geophysical Research* 81:1217–1230.
- Shoemaker E. M. 1962. Interpretation of lunar craters. In *Physics and astronomy of the Moon*, edited by Kopal A. New York: Academic Press. pp. 283–351.
- Shuvalov V. V., Svetsov V. V., and Trubetskaya I. A. 2013. An estimate for the size of the area of damage on the Earth's surface after impacts of 10–300-m asteroids. *Solar System Research* 47:260–267.
- Svetsov V. V., Nemtchinov I. V., and Teterov A. V. 1995. Disintegration of large meteoroids in Earth's atmosphere: Theoretical models. *Icarus* 116:131–153.
- Svetsov V. V. 2007. Estimates of the energy of surface waves from atmospheric explosions and the source parameters of the Tunguska event. *Izvestiya, Physics of the Solid Earth* 43:583–591.
- Toon O. W., Zahnle K., Morrison D., Turco R. P., and Covey C. 1997. Environmental perturbations caused by the impacts of asteroids and comets. *Reviews of Geophysics* 35:41–78.
- Tsvetkov V. I. and Skripnik A. Y. 1991. Atmospheric fragmentation of meteorites according to the strength theory. *Solar System Research* 25:273.
- Weibull W. 1951. A statistical distribution function of wide applicability. *Journal of Applied Mechanics, Transactions ASME* 18:293–297.
- Wünnemann K., Collins G. S., and Melosh H. J. 2006. A strain-based porosity model for use in hydrocode simulations of impacts and implications for transient crater growth in porous targets. *Icarus* 180:514–527.

APPENDIX: ANALYTICAL APPROXIMATION TO THE ABLATIVE PANCAKE MODEL

The “Pancake model” (Chyba et al. 1993; Collins et al. 2005) describes the deceleration and deformation of a meteor in an atmosphere. It assumes that the meteor can be described as a strengthless cylinder which deforms under the differential pressure between the ram pressure on the front face and the essentially zero pressure of the meteor's wake. Ignoring the effects of gravity and lift, which are insignificant for most large meteors, the pancake model equations are given by:

$$\frac{dv}{dt} = -\frac{C_D \rho_a \pi L^2}{8m} v^2 \quad (\text{A1a})$$

$$\frac{dm}{dt} = -\frac{1}{8} K_H \rho_a \pi L^2 v^3 \quad (\text{A1b})$$

$$\frac{d^2 L}{dt^2} = \frac{C_D \rho_a}{\rho_i L} v^2 \quad (\text{A1c})$$

$$\frac{dz}{dt} = -v \sin \theta \quad (\text{A1d})$$

In A1, v , m , L , and ρ_i are the meteoroid velocity, mass, diameter, and density, respectively; C_D is the drag coefficient; $\rho_a(z)$ the atmospheric density as a function of altitude z ; K_H is an ablation parameter equal to the ablation efficiency divided by the specific heat of ablation, θ the meteoroid trajectory angle to the surface, and t is time; all terms use MKS units.

Assuming a straight trajectory, appropriate when neglecting gravity and lift, these equations can be reformulated in terms of altitude to give:

$$\frac{dv}{dz} = -\frac{C_D \rho_a A}{2 \sin \theta m} v \quad (\text{A2a})$$

$$\frac{dm}{dz} = -\frac{K_H \rho_a A}{2 \sin \theta} v^2 \quad (\text{A2b})$$

$$L \frac{d^2 L}{dz^2} = \frac{C_D \rho_a}{\rho_i \sin^2 \theta} \quad (\text{A2c})$$

For simplicity, Collins et al. (2005) assumed no mass loss by ablation (i.e., $\frac{dm}{dz} = 0$) and found approximate analytical solutions to A2a and A2c. As ablative mass loss can be significant for small meteoroids, here we seek an approximate (semi-) analytical solution to A2. Before developing a general solution to this system of equations, we observe that the ablation parameter K_H provides a convenient way of nondimensionalizing the velocity term and define a nondimensional specific energy of the decelerating meteoroid for the ablative case:

$$\chi \equiv \frac{1}{2} \frac{K_H}{C_D} v^2 \quad (\text{A3})$$

For the ablationless case, this parameter is undefined and an alternative nondimensional specific energy that can be used instead is the meteoroid's residual kinetic energy as a fraction of the initial kinetic energy:

$$E_{kp} = \left(\frac{v}{v_0} \right)^2 \quad (\text{A4})$$

which we refer to as the kinetic energy partition. This can also be defined in the ablative case as:

$$E_{kp} = \left(\frac{\chi}{\chi_0} \right) \quad (\text{A5})$$

where χ_0 is the initial value of the nondimensional specific energy.

For the ablative case, combining Equations A2a and A2b gives an equation relating χ to the ratio of meteoroid mass to initial mass m_0 :

$$\ln \left(\frac{m}{m_0} \right) = \chi - \chi_0 \quad (\text{A6})$$

Lastly, we define an aerodynamic mass ratio M_R as the ratio of the mass of air swept out by the meteor along its path to the initial meteor mass. In differential form, this is given by:

$$\frac{dM_R}{dz} = -\frac{\rho_a A}{m_0 \sin \theta} \quad (\text{A7})$$

Defining M_R in this way enables all the atmospheric and deformation model terms to be contained in a single integral:

$$M_R = -\frac{1}{m_0 \sin \theta} \int_z^\infty \rho_a A dz \quad (\text{A8})$$

Combining Equations A2a, A3, A6, and A7 gives a single governing differential equation relating the nondimensional specific energy of the meteoroid χ to the atmospheric mass ratio M_R :

$$\frac{e^{\chi-\chi_0}}{\chi} \frac{d\chi}{dz} = C_D \frac{dM_R}{dz} \quad (\text{A9})$$

We note that for completeness Equation A9 could be nondimensionalized fully by dividing the altitude z by the atmospheric scale height H , but as this makes no difference to the form of the equation it is unnecessary here. The related ablationless equation is:

$$\frac{1}{E_{kp}} \frac{dE_{kp}}{dz} = C_D \frac{dM_R}{dz} \quad (\text{A10})$$

Integrating these equations from z to infinity gives relationships between the aerodynamic mass ratio and the nondimensional specific energy for the ablative and ablationless case, respectively, which are independent of assumptions about the atmospheric structure and deformation model, provided the deformation is independent of the instantaneous meteoroid mass and velocity:

$$\text{Ei}(\chi) = \text{Ei}(\chi_0) + C_D e^{\chi_0} M_R \quad (\text{A11a})$$

$$\ln E_{kp} = C_D M_R \quad (\text{A11b})$$

Note that $\text{Ei}(\cdot)$ is the “exponential integral,” which is straightforward to evaluate numerically in common maths packages. The inverse of the exponential integral is nontrivial to evaluate; however, for the range of values likely to be encountered for a physical impact a simple inversion scheme will suffice. Hence, Equation A11 can be evaluated to find the meteoroid speed at a given altitude by solving the integral in the definition of M_R (Equation A8) for plausible assumptions about atmospheric structure and meteoroid deformation. For an isothermal atmosphere:

$$\rho_a = \rho_s \exp(-z/H) \quad (\text{A12})$$

where ρ_s is the atmospheric density at the surface and H the scale height of the atmosphere (~ 8 km for Earth). In this case, the mass ratio for a nondeforming meteoroid is simply:

$$M_R = \frac{\rho_s A H}{m_0 \sin \theta} e^{-\frac{z}{H}} = \frac{A H}{m_0 \sin \theta} \rho_a(z) \quad (\text{A13})$$

where $A = \frac{1}{4} \pi L_0^2$ is the cross-sectional area of the meteoroid of constant diameter L_0 . In reality, even strong meteoroids fragment under aerodynamic stresses and subsequently deform. Hence, A13 applies only above z_* the fragmentation altitude—the altitude at which the strength of the meteoroid is exceeded and it starts to deform—which can be estimated using Equation 11 in Collins et al. (2005).

Adopting the Pancake model of meteoroid deformation (A2c) below the fragmentation altitude, the integral in the equation for the aerodynamic mass ratio can be rewritten as:

$$-\int_z^{z_*} \rho_a A dz = \frac{\pi}{4} \rho(z_*) \int_z^{z_*} L^2(z) e^{(z_*-z)/H} dz \quad (\text{A14})$$

Collins et al. (2005) found a good analytical approximation for the integral on the righthand side of A14:

$$\int_z^{z_*} L^2 e^{(z_*-z)/H} dz = \frac{l L_0^2}{24} \alpha [8(3 + \alpha^2) + 3\alpha \frac{l}{H} (2 + \alpha^2)] \quad (\text{A15})$$

where l is the dispersion length scale defined as $l = L_0 \sin \theta \sqrt{\frac{\rho_i}{C_{DP}(z_*)}}$ and

$$\alpha = \sqrt{\left(\frac{L(z)}{L_0}\right)^2 - 1} = \left(\frac{2H}{l}\right) \left[e^{(z_*-z)/2H} - 1\right] \quad (\text{A16})$$

Thus, for a meteoroid deforming according to the pancake model in an isothermal atmosphere the

aerodynamic mass ratio below the fragmentation altitude is:

$$M_R = \frac{\rho_a(z_*) \pi l L_0^2}{m_0 \sin \theta 96} \alpha [8(3 + \alpha^2) + 3\alpha \frac{l}{H} (2 + \alpha^2)] \quad (\text{A17})$$

which can be evaluated at any altitude below z_* using A16. At altitudes well below the fragmentation altitude ($z \ll z_*$), the mass ratio given by A17 is several orders of magnitude larger than the mass ratio at fragmentation, given by A13 evaluated at $z = z_*$ and hence the latter can be ignored. Otherwise, the total mass ratio is the sum of A13 evaluated at $z = z_*$ and A17. The Aerodynamic Mass Ratio can be defined for other models of meteor deformation or atmospheric structures (e.g., polytropes, International Standard Atmosphere, etc.).

The height of maximum energy deposition per km is an important quantity when determining the effects of the shockwave on the ground. This can be used to define the burst height z_b . For the ablationless case, this is the altitude at which the second derivative of E_{kp} is zero:

$$\frac{d^2 E_{kp}}{dz^2} \Big|_{z=z_b} = 0 \quad (\text{A18})$$

From this condition, it can be shown that for most scenarios of interest the kinetic energy partition at the burst height $E_{kp}(z_b) = e^{-1}$; i.e., at the burst altitude the residual kinetic energy of the meteoroid is approximately one-third of the initial kinetic energy. The equivalent condition for the ablative case is more complicated to analyze; however, for weakly ablative scenarios ($\chi_0 \sim 1$) typical of stony objects entering at 15–30 km s⁻¹, the kinetic energy partition at burst is also close to one-third.